Journal of Materials Chemistry C

Accepted Manuscript

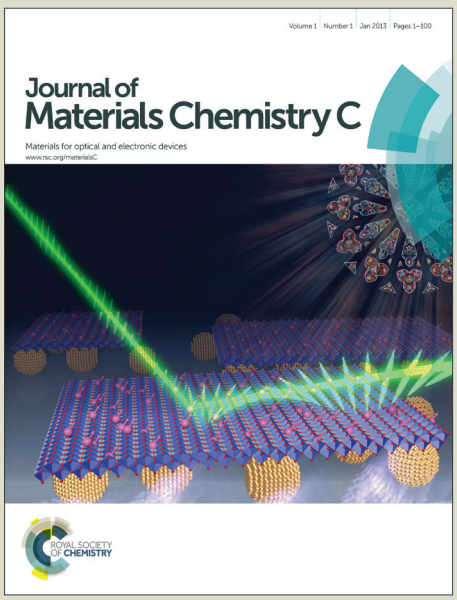

ROYAL SOCIETY OF CHEMISTRY

www.rsc.org/materialsC

Journal of Materials Chemistry C

RSCPublishing

ARTICLE

Nanocluster seed-mediated synthesis of $CuInS_2$ quantum dots, nanodisks, nanorods, and doped Zn-$CuInGaS_2$ quantum dots

Cite this: DOI: 10.1039/x0xx00000x

Received 00th January 2012,
Accepted 00th January 2012

DOI: 10.1039/x0xx00000x

www.rsc.org/

Sanjaya D. Perera, Haitao Zhang, Xiaoyue Ding, Andrew Nelson, Richard D. Robinson

Cornell University, Department of Materials Science and Engineering, 214 Bard Hall, Ithaca, New York 14853, United States

Recent work using seed-mediated quantum dot growth has shown that nanoparticle seeds are a useful method for providing nucleation centers in order to control the nanoparticle shape and composition. Here we present a facile nanocluster seed-mediated protocol to synthesize $CuInS_2$ quantum dots (q-dots) and Zn and/or Ga doped $CuInS_2$ (Zn-$CuInGaS_2$) q-dots using $(NH_4)_2S$ as a sulfur source. Due to high reactivity of $(NH_4)_2S$ toward metal cations, we are able to isolate a $CuInS_2$ nanocluster (<2 nm with low crystallinity) intermediate at low temperatures (60 ^oC). By varying the conditions of a "heat-up" synthesis method, these nanoclusters can be grown into $CuInS_2$ with different morphologies (q-dots, nanodisks, and nanorods) and different crystalline phases (chalcopyrite and wurtzite). Further, we can incorporate dopant Ga^{3+} and Zn^{2+} ions into the q-dots by introducing the dopant either during the nanocluster formation or during the crystal growth stage, resulting in $CuInGaS_2$ and CuInZnS q-dots. Incorporation of both Ga and Zn increases the photoluminescence intensity compared to $CuInS_2$; furthermore, the absorption spectra and photoluminescent emission peaks are shifted to shorter wavelengths. With this method, we have also accomplished the synthesis of pentanary Zn-$CuInGaS_2$ for the first time. Compared to quaternary $CuInGaS_2$ and CuInZnS, we observed a larger blue shift in the absorption spectra when both Zn and Ga are present. The interesting optical properties of Zn-$CuInGaS_2$ make them an attractive material for photovoltaic devices and light emitting diodes. The ability to isolate the intermediate $CuInS_2$ nanoclusters provides a strategy for synthesizing a wide variety of tailored quaternary and pentanary metal chalcogenides in the future.

Introduction

Colloidal semiconducting nanocrystals have attracted great attention due to their unique physical and chemical properties.[1-4] Among the broad range of semiconductor nanocrystals, metal chalcogenides have received ample interest for application in photovoltaic,[5] photocatalytic,[6] electrochemical and biomedical applications.[7,8] Tremendous efforts have been devoted to synthesize II-VI semiconductor nanoparticles, such as CdS,[9] CdSe[10,11] and CdTe[12], due to their fluorescence properties with high quantum yields and tunable emission wavelengths, leading to their prominent use in light emitting diodes (LEDs)[4] and photovoltaics.[13,14] Although CdSe and CdTe nanoparticles have shown excellent optical properties, new Cd-free metal chalcogenides are being sought for applications that require environmentally friendly and low cost alternatives to Cd.

Ternary chalcogenides (I-III-VI_2) based on the sulfides, selenides and tellurides of Cu, Ag, and Zn, combined with Al, Ga, and In, have been identified as nanomaterials with promising optical properties, particularly for light absorption matching the solar spectrum.[15-17] Recently, materials having mixed $Cu(In,Ga)(S,Se)_2$ composition have attracted attention for photovoltaic and photocatalytic hydrogen evolution applications.[5,17-19] Among the different forms of Cu-chalcogenides, copper indium sulfide ($CuInS_2$) is a particularly promising candidate due to its wide range of tunability in optical and chemical properties.[20,21] $CuInS_2$ is a direct band gap semiconductor and has a relatively narrow band gap (1.5 eV) with a high absorption coefficient (10^{15} cm^{-1}).[22,23] Due to these interesting features, $CuInS_2$ has shown great potential in photovoltaics and LED applications.[24-26]

A variety of chemical synthesis methods have been developed to synthesize $CuInS_2$, including hydrothermal,[27] microwave,[28] hot-injection,[29] and heating-up[30] syntheses. The properties of $CuInS_2$ can be fine-tuned for a particular application by changing the chemical composition and by adjusting the morphology. The seeded growth approach has also been successfully applied to fabricate colloidal nanocrystals with a variety of morphologies.[10,31] Methods for changing the chemical composition of $CuInS_2$ include the introduction of defects,[30,32,33] doping,[34,35] and growing core-shell structures.[36,37] Although previous work has shown the synthesis of different $CuInS_2$ morphologies and phases,[28,38-43] the synthesis of $CuInS_2$ and quaternary metal chalcogenides remains challenging due to the different reactivity of metal cations towards the anion precursor. This is mainly overcome by selecting suitable types of ligands (leaving groups) and solvents.[42] However complications arise in typical synthetic protocols for $CuInS_2$ using Lewis base type solvents (e.g., dodecanethiol) run at high temperatures (most commonly above 200 ^oC.[32,42]) Nanocrystals of chalcopyrite compounds have also been synthesized via thermal decomposition of single-source or double-source molecular precursors.[20,44,45] One precursor to enable a rational synthesis for metal chalcogenides is $(NH_4)_2S$, as previously demonstrated by our group.[46] Compared to organic thiols and elemental sulfur, $(NH_4)_2S$ acts as a more reactive sulfur source.[46] While almost all reported synthetic routes have focused on high temperature conditions, using $(NH_4)_2S$ we were able to synthesize high quality metal chalcogenide nanocrystals at considerably lower temperatures.[46] The reaction scheme is particularly attractive since the synthesis involves a scalable, low temperature heat-up method.[47]

Research into $CuInS_2$ has been directed toward the introduction of cations such as Ga, Zn, Ag, Sn and Mn to derive interesting quaternary chalcogenides with tunable optical properties. [34,48-53] Doping or alloying of $CuInS_2$ is achievable by refluxing the $CuInS_2$ nanocrystal product with the guest cation.[49] For scalability towards industrial applications, a one-pot synthesis technique is a key goal; however, the challenge with conventional one-pot synthesis routes is that as the number of cationic precursors increases, difficulty to solvate cationic species in organic solvents becomes more challenging. Incorporating a large number of different cations into a one pot synthesis can be expected to be far more challenging when preparing quaternary and possible pentanary chalcogenides.

As an alternative to the typical one-pot colloidal syntheses or hot injection techniques, the preparation of nanoclusters or molecular clusters of ternary chalcogenides is a successful approach to obtain control to incorporate cations. Cluster-based molecular compounds are an important class of intermediates, which provide a distinct atomic environment for doping and structure evolution.[54] However, only a few reports are available on the study of heterometallic thiolate clusters, especially with respect to their use for nanocrystal growth. For example, Cu-In thiolate,[55] and $[Cu_{6-x}Au_x(SCH_2CH_2S)_4]^{2-}$ $[Ag_{6-x}Au_x(SCH_2CH_2S)_4]^{2-}$ clusters[56] have been reported. Recently, Feng *et al.* demonstrated a two-step strategy to prepare Cd-In-S supertetrahedral nanoclusters and to dope them with Cu.[54] Manna and co-workers prepared Cu-In-Zn-S nanocrystals by partially exchanging cations of $Cu_{1-x}InS_2$ with Zn.[33] To date, the preparation of monomeric $CuInS_2$ nanoclusters and their potential for crystallization and incorporation of guest cations as a means to forming Zn-$CuInGaS_2$ nanocrystals has not been reported. Discovery of synthetic protocols for monomeric Cu-In-S clusters could lead to new materials and methods for the creation of novel nanomaterials.

In this study, we introduce a novel two-step synthetic protocol to prepare $CuInS_2$ nanocrystals, and Zn and/or Ga doped $CuInS_2$ nanocrystals. In the first step, $CuInS_2$ nanoclusters (<2 nm) are prepared and separated. These isolated, poorly crystalline $CuInS_2$ nanoclusters are subsequently aged under different synthetic conditions to grow crystalline nanoparticles. The nanoclusters can be converted to q-dots, nanodisks, and nanorods by simply varying the heat-up temperature rate and by introducing TOP (tri-*n*-octylphosphine). TOP effectively regulates the particle formation to form two-dimensional disks. At faster temperature ramp rates, the $CuInS_2$ clusters undergo a phase transformation from chalcopyrite $CuInS_2$ to wurtzite $CuInS_2$. The $CuInS_2$ nanocluster can be doped into a crystalline quaternary (Zn, Ga)-$CuInS_2$ that exhibits higher PL intensities and a blue shift in absorption spectra. Our current work, therefore, highlights not only the ability to use a nanocluster seed method to nucleate and grow $CuInS_2$ into different shapes and crystal phases, but also the ability to induce defects and incorporate cations during both the cluster formation and nucleation stages. The as-prepared $CuInGaS_2$ exhibits a blue shift in its optical absorption spectrum and an increase in its photoluminescence intensity. Further incorporation of Zn shows an even more significant blue shift in absorption spectra. Herein, we report the synthesis of pentanary colloidal Zn-$CuInGaS_2$ in the chalcopyrite phase using a two-step reaction scheme for the first time. We find that the presence of Ga and/or Zn in Zn-$CuInGaS_2$ strongly affects the photoluminescence and optical absorption properties.

Experimental

Materials and characterization

Hexanes (≥ 98.5%), ethanol (≥ 99.5%), (90%), 1-dodecanethiol (98%) (DDT), ammonium sulfide (40-48 wt% solution in water), oleylamine (70%) (OLA), trioctylphosphine (97%) (TOP), copper(I) chloride (99.995%), indium(III) chloride (99.999%), gallium(III) chloride (99.999%) and zinc(II) chloride (99.999%) were purchased from Aldrich; molecular sieves (UOP type 3 Å) were purchased from Aldrich and activated at 300 ^oC under dynamic vacuum for 6 hours before use. Experiments were carried out under a nitrogen atmosphere by employing standard Schlenk line techniques.

Transmission electron microscopy (TEM) images were recorded on an FEI Tecnai T12 transmission electron microscope operating at 120 kV; the high-resolution TEM (HRTEM) images were collected on an FEI Tecnai F20 transmission electron microscope operating at 200 kV. A Bruker General Area Detector Diffraction System (GADDS) (Cu Kα radiation) was employed to record X-Ray diffraction data using a HI-STAR detector. UV-vis absorption data were collected on an Ocean Optics USB2000+VIS-NIR, using a deuterium source (210-400 nm). Photoluminescence (PL) data were recorded using the same spectrometer using UV LED light source (excitation wavelength 240 nm). XPS analysis was performed using a Surface Science Instruments SSX-100 with operating pressure ~$2x10^{-9}$ Torr. Monochromatic Al Kα x rays (1486.6 eV) were used with beam diameter of 1 mm. Photoelectrons were collected at a 55-degree emission angle. A hemispherical analyzer determined electron kinetic energy, using a pass energy of 150 V for wide/survey scans, and 50V for high resolution scans. A flood gun was used for charge neutralization of non-conductive samples.

Synthesis of $CuInS_2$ nanoclusters

In a typical synthesis, a mixture of 0.54 g copper(I) chloride and 0.129 g of indium(III) chloride was dissolved in 10 mL DDT, followed by heating at 80 ^oC until the solution became clear. The temperature was then lowered to 60 ^oC, and molecular sieve-dried $(NH_4)_2S$ in OLA solution (4 mL, 0.5 mmol/mL) was injected. The mixture turned dark brown-red immediately. The heating source was then removed and the mixture was allowed to cool down to room

temperature. Ethanol was added to the solution to precipitate the $CuInS_2$ nanoclusters, which were isolated by centrifugation.

Synthesis of $CuInS_2$ quantum dots, nanodisks and nanorods

In order to synthesize $CuInS_2$ quantum dots (q-dots), the nanocluster precursor was dispersed in 5 ml of DDT. After degassing and purging with N_2, the solution was heated to 145 ^oC at a ramping rate of 3 ^oC/min with magnetic stirring. Once the temperature reached 145 ^oC, the solution was directly introduced into 25 mL of ethanol and stirred at room temperature to quench the reaction. As-prepared $CuInS_2$ quantum dots were separated by centrifugation. To form $CuInS_2$ nanodisks, the nanoclusters were dispersed in a mixture of 5 mL of DDT and 250 μL of TOP and followed the same procedure as described for the synthesis of nanoparticles. $CuInS_2$ nanorods were formed by dispersing $CuInS_2$ nanoclusters in 5 mL of DDT and heating to 160 ^oC at a ramping rate of 10 ^oC/min. At 160 ^oC, the reaction solution was immediately quenched by introducing to 25 mL of ethanol. The product was separated by centrifugation.

Synthesis of CuInZnS

$CuInS_2$-nanoclusters were prepared as described in the previous step using 0.45 mmol of copper (I) chloride and 0.5 mmol of indium(III) chloride. Prior to dispersing the monomer, the desired amount of zinc(II) chloride was dissolved in 5 mL of 1-dodacanethiol by heating the solution to ca. 80 ^oC. Then the temperature was lowered below ~50 ^oC and the solution was introduced to the crude $CuInS_2$ nanocluster precursor. The reaction mixture was heated to 145 ^oC (3 ^oC/min ramp rate). At 145 ^oC, the solution was immediately quenched by introducing 25 mL of ethanol, followed by centrifugation to separate the final product.

Synthesis of $CuInGaS_2$ via $CuInGaS_2$ nanocluster

The desired amount of gallium(III) chloride was dissolved in 5 mL of DDT at room temperature *($GaCl_3$ is readily soluble in DDT at room temperature)*. 0.5 mmol copper (I) chloride and 0.45 mmol of indium(III) chloride were added to the solution, which was then heated to 80 ^oC until the solution became clear. The experimental steps for $CuInS_2$ nanocluster synthesis (see above) were followed to obtain $CuInGaS_2$ nanoclusters. Isolated nanoclusters were dispersed in 5 mL of DDT followed by heating to 145 ^oC at a ramping rate of 3 ^oC/min. At 145 ^oC the reaction was quenched using 25 mL ethanol, and the product was separated by centrifugation.

Synthesis of pentanary Zn-$CuInGaS_2$ via $CuInGaS_2$ nanoclusters

$CuInGaS_2$ nanoclusters were obtained as described earlier. The procedure described in the synthesis of CuInZnS was followed to introduce Zn. Briefly, zinc(II) chloride was dissolved in 5 mL of 1-dodacanethiol at ca. 80 ^oC. Once the temperature of the solution is below ~50 ^oC, $CuInGaS_2$ clusters were introduced, and the mixture was heated to 145 ^oC (3 ^oC/min ramp rate). At 145 ^oC, the solution was quenched by introducing 25 mL of ethanol. Zn-$CuInGaS_2$ was separated by centrifugation and re-dispersed in hexane. All samples were stored under nitrogen in a glove box**.**

Results and Discussion

Figure 1 shows a schematic diagram representing the overall reaction pathways for the synthesis of different $CuInS_2$ nanocrystals. In the first step the $CuInS_2$ nanocluster precursor is prepared. These cluster precursors are then grown to nanocrystals, such as quantum dots (q-dots), nanodisks and nanorods using different reaction conditions. Forming this reactive $CuInS_2$ nanocluster intermediate before the crystal growth facilitates the conversion of the clusters into nanocrystals of $CuInS_2$ with different morphologies (spheres, nanorods, and nanodisks). Nanodisks are formed by introducing a capping agent before the growth stage, while nanorods are formed by increasing the heating rate and growth temperature. Use of a nanocluster intermediate also facilitates the introduction of dopant cations (Zn^{2+} and Ga^{3+}) into the nanocluster. Introducing dopants during the nanocluster formation stage allows the facile incorporation of the dopant ions into the nanoclusters, and these ion-incorporated nanoclusters then facilitate the formation of doped nanocrystals during the growth stage. This method is thus an attractive and flexible synthesis route to prepare complex chalcogenides, such as pentanary Zn-Ga-$CuInS_2$. During each reaction stage, Zn and Ga can be incorporated to form CuInZnS, $CuInGaS_2$, and Zn-$CuInGaS_2$.

The morphology of the nanoclusters was investigated by transmission electron microscopy. The cluster precursor shows nanoclusters with a low crystallinity, which is confirmed by both TEM and XRD analysis. TEM images of $CuInS_2$ nanoclusters do not show any special morphology (Figure 2a). However, the non-aggregated, isolated $CuInS_2$ nanoclusters visible in TEM are <2.0 nm in size. We believe that the reaction between the precursors for the monomers forms a metal complex or nanocluster, which subsequently grows into the crystalline product upon heating. The low crystallinity of the nanoclusters is further evidenced by the low intensity and broadness of XRD peaks (Figure 2b). Based on XRD, the average grain size of the $CuInS_2$ nanoclusters calculated using the Debye–Scherrer equation is about 1.61 nm, which is consistent with TEM observations. XRD patterns of the intermediate nanoclusters match with the characteristic peaks of the tetragonal chalcopyrite structure. However, it is possible that polytypic $CuInS_2$ possessing both the tetragonal and hexagonal phases exists within the nanoclusters. Previous studies have also reported the formation of polytypic nanoparticles during $CuInS_2$ synthesis.[5] UV-vis spectroscopy was used to further analyze the intermediate $CuInS_2$ nanoclusters and nanocrystals Figure s1a shows the UV-vis absorption spectrum of as-prepared nanoclusters, which features a broad absorption in the visible region.

To investigate the formation of the $CuInS_2$ nanoclusters, several nanoclusters were prepared with varying molar ratios of Cu:In in DDT. Results of this study show the solubility of the CuCl and $InCl_3$ mixture significantly decreases as the molar ratio deviates from 1:1, i.e., when the Cu:In molar ratio is greater than 1, the mixture is insoluble at 60 ^oC (the reaction temperature required to form clusters). This implies that a stoichiometric quantity of indium is necessary to create a stable, soluble Cu-In-thiol complex. To investigate the effect of the presence of In^{3+} on the formation of $CuInS_2$, we prepared three different Cu:In molar ratio mixtures in DDT (1:0.25, 1:0.5, 1:0.75 and 1:1). The 1:1 molar ratio mixture of CuCl and $InCl_3$ is a clear solution, even at room temperature, while the other mixtures (1:0.25, 1:0.5, 1:0.75 molar ratios of CuCl to $InCl_3$) are not soluble in DDT below 85 ^oC. Typically, CuCl and $InCl_3$ are also not soluble in DDT at room temperature. Figure s1a inset image shows a comparison of solubility of (I) CuCl, (II) $InCl_3$, (III) a Cu-In mixture (1:1 molar ratio). This implies that a stoichiometric molar ratio of Cu:In is necessary for solubility of CuCl and $InCl_3$ in DDT. It is likely that the 1:1 molar ratio forms a complex that has much higher solubility.

Similar to previous studies, as-synthesized $CuInS_2$ nanoclusters typically show a deep brown-red color (Figure s1a-IV).[30] XRD patterns of the nanoclusters with a 1:1 Cu:In molar ratio (Fig. 2c,I) show nearly identical characteristics to the $CuInS_2$ XRD patterns reported in literature.[30, 57-59] In contrast to the 1:1 Cu:In molar ratio nanoclusters, the XRD patterns of the other stoichiometries show a mixture of $CuInS_2$, CuS, and Cu_7S_4 (Figure s1b). In the XRD of these sub-stoichiometric Cu:In mixtures, the peak intensity

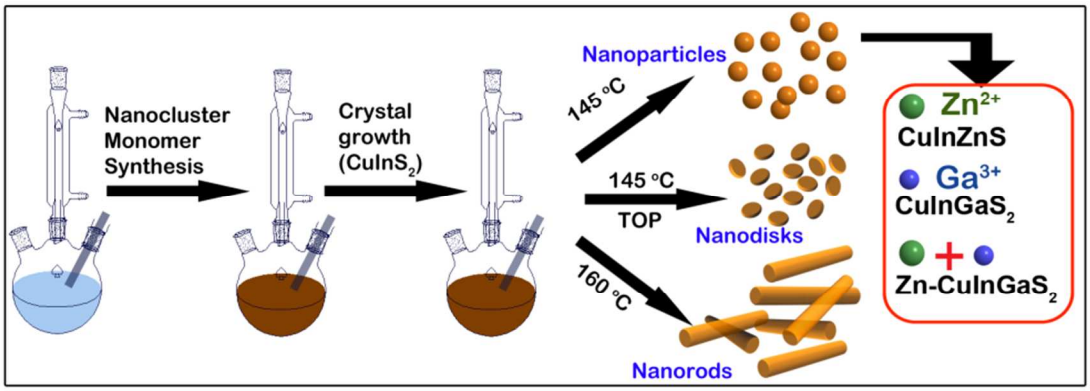

Figure 1. Schematic diagram showing the synthesis of $CuInS_2$ quantum dot nanoparticles, nanodisks and nanorods using $CuInS_2$ nanoclusters, and the incorporation of Zn and Ga to synthesize CuInZnS, $CuInGaS_2$ and Zn-$CuInGaS_2$.

of the major $CuInS_2$ (112) reflection decreases and the peaks corresponding to copper sulfides become stronger as the molar ratio of Cu:In ratio increases. The (112) reflection is completely absent in the 1:0.25 sample, indicating that $CuInS_2$ does not form. Despite the presence of $InCl_3$, the XRD patterns of the sub-stoichiometric Cu:In samples indicate these Cu-rich samples are mainly a mixture of CuS and Cu_7S_4, as suggested in a previous report.[60] These observations suggest that the nanoclusters prepared with the stoichiometric molar ratio mainly consist of a $CuInS_2$ phase.

The formation of $CuInS_2$ clusters was further evaluated by annealing dry, isolated $CuInS_2$ nanoclusters in air at various temperatures. $CuInS_2$ nanoclusters exhibit very poor crystallinity, leading to broad XRD peaks. Thus, the evolution of the XRD patterns of annealed nanoclusters can provide more evidence for the formation of $CuInS_2$ during the cluster formation stage. Figure 2c shows the XRD patterns of $CuInS_2$ nanoclusters annealed at different temperatures. The results of the annealing show that clusters annealed at 200 ^oC exhibit well-resolved peaks corresponding to $CuInS_2$ (JCPDS file: 00-047-1372). The increased intensity of the (204) and (312) peaks can be attributed to the increased crystallinity of $CuInS_2$ phase. These results indicate that the synthesis of $CuInS_2$ nanocrystals proceeds via a $CuInS_2$ nanocluster intermediate stage. To further confirm the formation of intermediate $CuInS_2$ nanoclusters, XPS analysis was performed on nanocluster samples that were isolated and purified immediately after the cluster formation. Figure 2d and 2e show the XPS spectra of Cu 2p and In 3d core electrons, respectively. The binding energies of Cu 2p 3/2 and Cu 2p 1/2 correspond to the Cu^+ oxidation state. Additionally, the binding energies of In 3d 3/2 and In 3d 5/2 are also in agreement with the In^{3+} oxidation state. The XPS data thus confirms that isolated nanoclusters mainly consist of $CuInS_2$.

Further information on the chemical properties of the nanoclusters and nanocrystals was obtained using FT-IR (Figure s1c). Sharp bands at 2916 cm^{-1} and 2849 cm^{-1} can be assigned to the asymmetric methyl stretching and asymmetric and symmetric methylene stretching vibrations, respectively.[61] By comparing the FT-IR spectra of nanoclusters and q-dots with those of OLA and DDT, it was found that compared to pure DDT, the absence of S-H vibration at 2573 cm^{-1} in both the nanoclusters and the final product suggests that metal-S bonds form upon introduction of $(NH_4)_2S$ dissolved in OLA.[61] The peak at 650 cm^{-1} is attributed to the stretching vibration of C-S bond of DDT. Compared to DDT, in $CuInS_2$ q-dots the C-S stretching vibration is shifted to lower wavenumbers, suggesting that DDT interacts strongly with the $CuInS_2$ cluster and the nanocrystal. The second step of the reaction (growth stage) was carried out using DDT as the solvent. The FT-IR spectrum of the $CuInS_2$ nanoclusters (Figure s1c) shows strong peaks in the range of 1540-1710 cm^{-1} and 1382 cm^{-1}, which can be attributed to the N-H bending mode and C-N stretching mode of OLA respectively.[62] This implies that the clusters are capped with OLA introduced via the ammonium sulfide solution. The absence of these lines in the spectra of nanocrystals, however, indicates that the OLA has been displaced by DDT during the crystal growth step. Because the second stage of the synthesis is performed in DDT as the solvent, the OLA capping the $CuInS_2$ is easily removed by DDT during nanocrystal aging.

Our two-step reaction is necessary to form the different morphologies because surfactant interactions with the precursors play a key role in controlling shape. We observed that excess OLA (from the ammonium sulfide solution) prevented the formation of nanorods. Thus, the excess OLA was removed from the system by precipitating the nanoclusters before aging them to form nanocrystals. For nanodisks, TOP is a necessary capping agent. We found, however, that TOP cannot be included in a one-pot method (i.e., synthesis without the nanocluster separation steps) because it decreases the solubility of the metal chlorides, presumably via unwanted side reactions, preventing the formation of nanoclusters. Therefore, the use of a nanocluster separation stage allows the later introduction of TOP and removal of excess OLA. This permits the growth morphology to be tuned. To form spherical q-dots, a linear and slow, linear heating rate of the reactive nanoclusters was used (145 ^oC at a rate of 3 ^oC/min). Figure 3 shows the TEM images of $CuInS_2$ q-dots, nanodisks and nanorods. The size distribution and average diameter of the q-dots were determined by analyzing TEM images acquired in several locations of the TEM grid. The $CuInS_2$ q-dots have an average diameter of 6.62 ± 0.93 nm (Figure 3a, inset image shows the distribution curve). The $CuInS_2$ nanodisks were synthesized under the same temperature conditions as the synthesis of spherical q-dots but in the presence of TOP. TEM images (Figure 3b) of nanodisks clearly represent the disk shape of the as-synthesized $CuInS_2$. These $CuInS_2$ nanodisks exhibit an average diameter of 6.94 ± 0.78 nm (Figure 3b, inset) and thickness of 2.90 ± 0.56 nm (Figure s2). The nanodisks are randomly oriented and do not tend to aggregate on the TEM grid likely due to the presence of the capping agent and the presence of thiol groups on the surface. Nanodisks lying flat over on the substrate show a circular shape; whereas the nanodisks that are standing on their sidewalls, where the basal facets are parallel to the electron beams, appear as an oval-shaped. The face-to-face assembling of nanodisks is a characteristic feature for moderate surface coverage of particles, while at higherconcentrations disks tend to arrange into arrays. The diameter of both the nanodisks and q-dots are not significantly different from

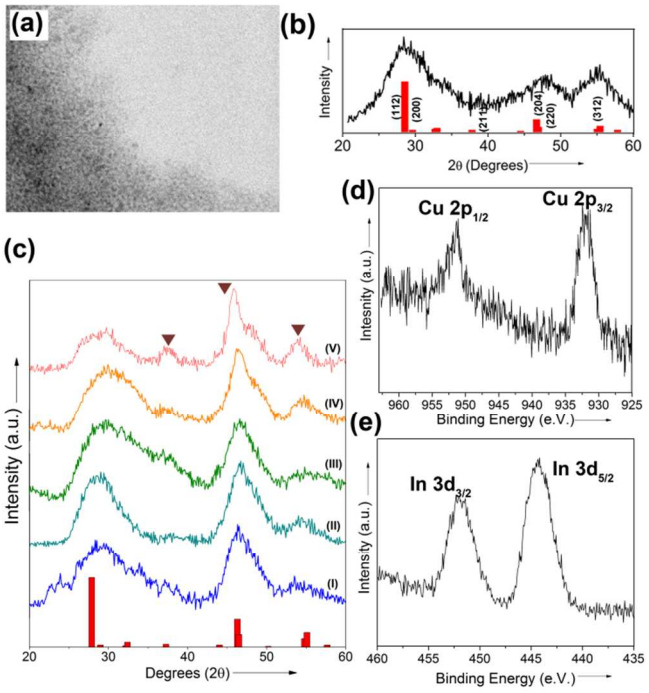

Figure 2. Characterization of $CuInS_2$ nanocluster monomer: a) TEM image, b) XRD pattern, c) XRD patterns of as prepared $CuInS_2$ nanoclusters (I), after annealing at 50 °C (II), 100 °C (III), 150 °C (IV) and 200 °C (V) for 1h. Triangles identify the characteristic peaks corresponding to the (204) and (312) reflections of $CuInS_2$, which become more intense after annealing. The stick pattern gives the reference lines for $CuInS_2$ (JCPDS 00-047-1372). XPS data for $CuInS_2$ nanoclusters showing (d) Cu 2p and (e) In 3d core electrons.

each other, which suggests that the TOP preferentially binds to certain facets and restricts growth on those faces. To convert the $CuInS_2$ nanoclusters into $CuInS_2$ nanorods, a faster heating rate of 10 °C/min to a higher final temperature (160 °C) is needed, compared to spherical and nanodisk forms which employ final temperatures of 145 °C at a heating rate of 3 °C/min (Figure 3c). To further confirm the disk shape morphology of $CuInS_2$, high-resolution transmission electron microscopy (HRTEM) together with sample tilting was carried out. Figure 3d shows an HRTEM image of a $CuInS_2$ nanodisk isolated from the colloidal suspension. HRTEM images clearly indicate the two-dimensional disk-like morphology and show lattice planes of 0.32 nm and 0.30 nm, corresponding to (112) and (103) crystal planes. The morphology of the nanodisks was studied by tilting the samples in the TEM. TEM images before and after tilting (Figure 3e and f, respectively) clearly suggest that $CuInS_2$ nanodisks represent a two dimensional, flat plate-like structure; the circled areas of the TEM images show the change in orientation upon tilting.

The XRD patterns (Figure 4a) of q-dots, nanodisks and nanorods were further analyzed to understand the structural change of $CuInS_2$ under different reaction conditions. Both the q-dots and nanodisks show the typical diffraction feature of tetragonal chalcopyrite materials, which matches with the Joint Committee on Powder Diffraction Standards (JCPDS) No. 27-0159. The diffraction peaks around 2θ = 27.9°, 32.38°, 37.2°, 46.2°, 55.1° can be correlated to the (112), (200), (211), (204) and (312) lattice planes, respectively. No diffraction peaks appeared in any of the samples corresponding to impurities such as CuS, Cu_2S, Cu_7S_4 or In_2S_3, confirming that the $CuInS_2$ nanoparticles, nanodisks and nanorods are of high purity. The XRD pattern obtained for nanorods are characteristic of the hexagonal wurtzite structure (Figure 4a, III), as opposed to the tetragonal chalcopyrite structure that was observed for q-dots and nanodisks. The well-defined diffraction peak observed at 2θ = 27.7°, which corresponds to the (112) plane, shows the highest intensity, suggesting that the growth direction of nanorods is along the *z*-axis ([001] direction). The phase of the final $CuInS_2$ crystalline product is strongly determined by the nucleation stage.[22] Previous work has shown that the different coordination properties and bond strengths between the nanoclusters and ligand molecules determine the stable phase selection.[22,63] The nanoclusters obtained at low temperatures (60 °C) have a tetragonal phase. Transformation of the tetragonal phase to wurtzite in the nanorods occurs after heating the nanoclusters in the nucleation and crystal growth stages. Since we prepared the $CuInS_2$ nanoclusters at low temperature and then cooled them down to room temperature, the nucleation of the tetragonal chalcopyrite phase must be fast and have a moderate growth rate. This clearly explains the existence of the tetragonal phase for q-dots and nanodisks, which form at a moderate heating rate at 145 °C. This observation also indicates that, compared to the tetragonal phase, the nucleation rate of the wurtzite phase formation is slower, but its growth rate is faster. Therefore, high growth rate conditions are required to form wurtzite $CuInS_2$. Similar growth trends were observed by Shinya and co-workers when using ligands with different binding strengths.[22] Recent studies have found that pre-nucleation clustering of monomers contributes to crystallization processes in colloidal nanocrystals.[64] In the present study, however, only one ligand (DDT) is present. Therefore, our main controls on the phase transformation are the heating conditions. At slow rates (3 °C/min) and lower maximum temperatures (145 °C) the total reaction time for the nucleation and growth through the entire process is longer than that for syntheses performed using a faster ramp rate (10 °C/min to 160 °C). As previously reported in $CuInS_2$ nanocrystal syntheses, at slower rates the nanoclusters have more time to form nuclei, and a larger portion of the $CuInS_2$ nanoclusters become consumed in the nucleation stage.[63] Due to the depletion of the nanocluster precursors in the nucleation stage, the rate of the growth stage is expected to be slow, leading to the formation of the more thermodynamically stable chalcopyrite $CuInS_2$ phase. However, faster heating rates, lead to shorter reaction times, which suppresses the consumption of nanoclusters during the nucleation step, leaving a larger amount of cluster precursor for the growth step. Therefore, a high growth rate can be expected, and the kinetically stable wurtzite $CuInS_2$ phase is formed. It should be noted that the critical point for this phase transformation is the nucleation stage and not the growth stage. Once the crystal phase is established, the crystal growth step is responsible for increasing the particle size or changing the shape.[63] Based on XRD analysis, the presence of the (200) peak corresponding to the tetragonal phase suggests that the nanorods also consist of trace amounts of tetragonal $CuInS_2$ phase. Moreover, the intensity ratio of XRD peaks, which have closer 2θ angles, i.e. (002), (110) and (112), to the intensity of (101) is higher than the simulated XRD pattern. This is also evidence for the presence of a minority chalcopyrite phase within nanorods. Similar results were previously observed for hexagonal $CuInS_2$ nanodisks, which contains domains of chalcopyrite $CuInS_2$.[22] These results suggest that the nanorods also possess a similar polytypic crystal phase.[43] The evolution

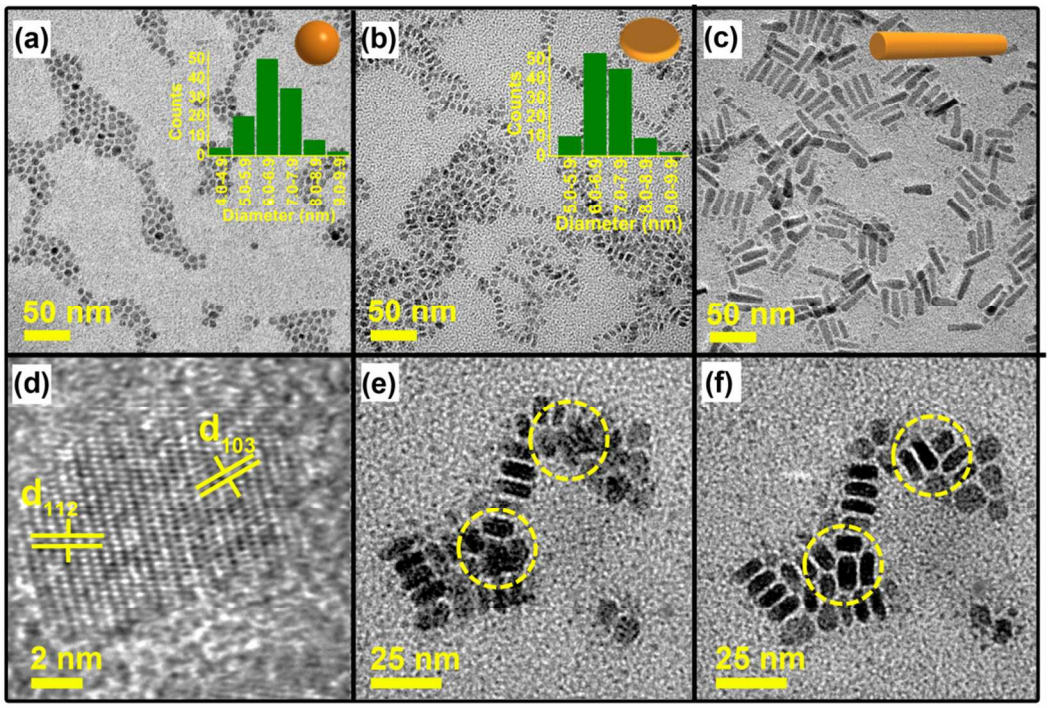

Figure 3. TEM images of $CuInS_2$ (a) nanoparticle spheres (q-dots), and (b) nanodisks, and (c) nanorods. Inset images to (a,b) show the size distributions of the q-dots (6.62 ± 0.93 nm) and nanodisks (diameter: 6.94 ± 0.78 nm, and thickness: 2.90 ± 0.56 nm). d) High resolution TEM image of a $CuInS_2$ nanodisk. Tilted TEM images (d) before and (e) after tilting the sample in 40° angle along x-axis confirm the disk shape of the nanodisks. Circled areas of TEM images represent $CuInS_2$ nanodisks whose change of orientation after tilting is easily identified.

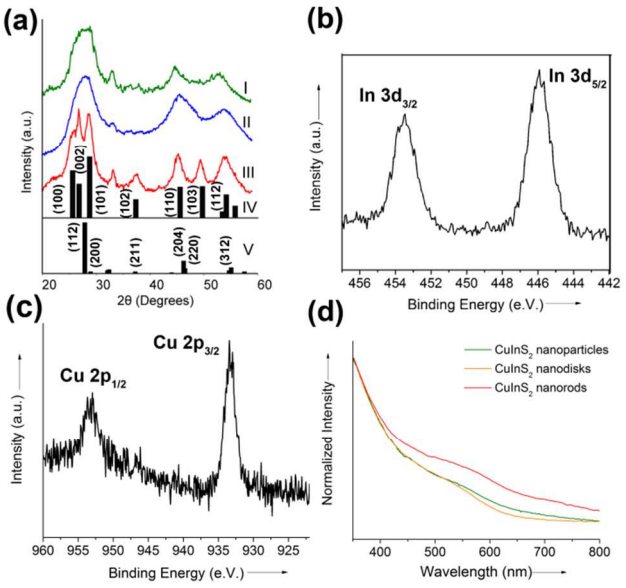

Figure 4. a) X-ray diffraction patterns of $CuInS_2$ q-dots (I), nanodisks (II) and nanorods (III). The reference patterns are for wurtzite (JCPDS 27-0159) (IV) and simulated chalcopyrite (V). XPS data for $CuInS_2$ nanodisks showing (b) In 3d and (c) Cu 2p core electrons. d) UV-vis absorption spectra of $CuInS_2$ nanocrystals with different morphologies.

of different morphologies of $CuInS_2$ was studied by annealing aliquots withdrawn during the growth stage (Figure s3). From the aliquot studies of the nanoparticles, we observed that, as the temperature increases to 75 ^oC, the nanoclusters aggregate to form q-dots with a diameter of ~5 nm. At 90 ^oC, Ostwald ripening occurs, dissolving the smaller nanocrystals and growing larger particles with diameters up to 25 nm. With subsequent heating to 125 ^oC and 135 ^oC, however, a transition to digestive ripening occurs, and the size distribution of the particles narrows. From the aliquot studies of the nanodisks, it appears that they also form through a lower-temperature Ostwald ripening stage followed by digestive ripening. During the synthesis of nanorods, as the reaction time progresses and the rate of heating increases, the $CuInS_2$ nanoclusters grow into nanoparticles, whose sizes increase with temperature up to 125 ^oC. The particles then begin elongating into nanorods (Figure s3). According to the aliquot study, this elongation occurs primarily at high temperatures (160 ^oC).

The valence states of Cu and In in nanodisks were investigated by XPS. The peaks centered at binding energies of 444.7 and 452.2 eV are due to the splitting of In 3d core electrons into $3d_{5/2}$ and $3d_{3/2}$ states, respectively (Figure 4b). This feature is well matched with In(III). Figure 4c shows a high-resolution XPS spectrum of Cu 2p spectrum, which consists of two peaks at 932.6 eV and 952.6 eV corresponding to the Cu $2p_{3/2}$ and Cu $2p_{1/2}$ core electrons. The splitting of the two peaks by 19.6 eV is in good agreement with the Cu(I) oxidation state. It has been shown that the Cu(II) oxidation state usually introduces a satellite peak at 942 eV, corresponding to Cu $2p_{3/2}$.[65] The absence of this 942 eV satellite peak in our samples is a clear indication of +1 oxidation state of Cu. XPS results therefore confirm that the as-synthesized samples consist of Cu(I) and In(III). Together, the XRD and XPS analyses confirm that the reaction yields high purity $CuInS_2$ nanocrystals without forming any Cu sulfide derivatives. The absorption spectra of $CuInS_2$ q-dot nanoparticles, nanodisks and nanorods are shown in Figure 4d.

The band gaps of the samples were obtained by the onset of the linear slope fitting at the start of absorption for each sample. It can be seen that the onset band gap for $CuInS_2$ is independent from the morphology of $CuInS_2$. The calculated onset band gaps for nanoparticles, nanodisks and nanorods are 1.96, 1.98 and 2.2 eV, respectively. For $CuInS_2$, the Bohr exciton radius is 4.1 nm, and thus quantum confinement can be observed in nanocrystals with characteristic dimensions of 8 nm and smaller.[66] The characteristic dimension of our nanoparticles, nanodisks, and nanorods are all within the quantum confinement regime.[67] There are no clearly distinguishable excitonic peaks in UV-vis spectra of our $CuInS_2$ nanocrystals.

We are able to dope the $CuInS_2$ nanocrystals by introducing the dopant atom either the first stage (creation of the nanoclusters) or the second stage (heating the nanoclusters into a nanocrystal). For the Zn doping we introduce Zn into the clusters during the heating-up step (the second stage in the process). When $ZnCl_2$ is added to the $CuInS_2$ nanoclusters and q-dots are grown, there is a sharp increase of the PL emission intensity. Upon introduction of Zn the PL intensity is enhanced by a factor of ~40 compared to $CuInS_2$ for samples having similar optical absorption at 400 nm. The intensity of the PL emission is directly correlated to the molar ratio of Zn/In. A TEM image of CuInZnS having a Zn/In precursor molar ratio of 0.5/1.0 is shown in Figure 5a.

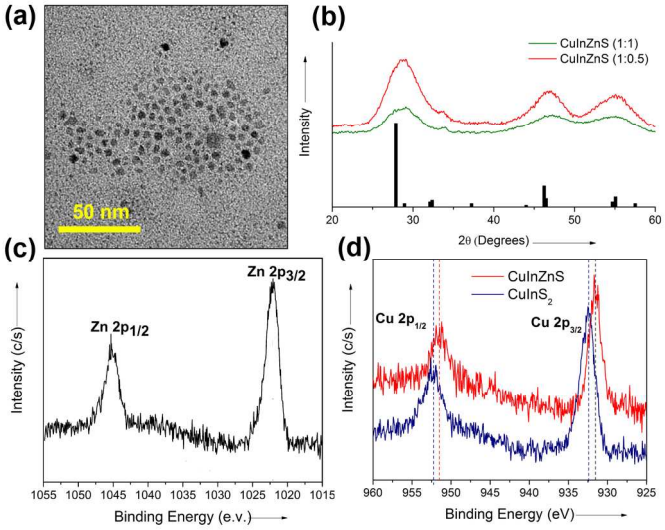

Figure 5. a) TEM image of CuInZnS nanoparticles. b) XRD patterns of CuInZnS with Cu:Zn ratio of 1:1 and 1:0.5. Overlayed stick patters shows reference peak positions of $CuInS_2$ (JCPDS 27-0159). XPS spectra of (c) Zn 2p core electrons and (d) Cu 2p core electrons for $CuInS_2$ and CuInZnS nanocrystals.

The diameter of these CuInZnS nanocrystals is 3.66 ± 0.25 nm. It is important to note that the nanocrystal size for the CuInZnS particles were were smaller than that of bare $CuInS_2$, suggesting that the atomic lattice was constrained upon the introduction of Zn to $CuInS_2$. This is likely because the ionic radius of Zn^{2+} (0.88 nm) is smaller than that of Cu^+ (0.91 nm) and In^{3+} (0.94 nm); thus Zn^{2+} can be readily incorporated to the $CuInS_2$ lattice structure.[26] XRD of the CuInZnS shows characteristic peaks corresponding to the chalcopyrite structure. Moreover, XRD patterns for CuInZnS shows a systematic shift of 1.12° of (112) peak to a higher 2θ angle; this shift is more evidence for incorporation of Zn (Figure 5b). Another possibility is that core-shell CuInZnS structures form in the presence of excess Zn^{2+} during the crystal growth stage.[52]

XPS shows the characteristic Zn $2p_{1/2}$ and $2p_{3/2}$ peaks appearing at binding energies of 1045 eV and 1022 eV, respectively (Figure 5c). The peak splitting of 23.17 eV can be assigned to the spin-orbit coupling of Zn(II).[68] The peaks centered at binding energies of 444.7 and 452.2 eV are attributed to In (III); these electron energies are split into $3d_{5/2}$ and $3d_{3/2}$ levels (Figure s4).[40] Based on the atomic ratios obtained from XPS analysis, the addition of Zn atoms increased the Cu/In ratio, from ~1.3 to 1.4 suggesting that the replacement of In sites with Zn. The comparison of XPS spectra of Cu 2p electrons reveals the slight shift of the $2p_{2/3}$ and $2p_{3/2}$ peaks to a lower binding energy due to the interaction of Zn with the $CuInS_2$ lattice (Figure 5d).[26] The spin-orbit splitting of the two peaks corresponding to Cu 2p for both $CuInS_2$ and CuInZnS is 19.6 eV; this can be attributed to the Cu(I) oxidation state in $CuInS_2$.[68] These results suggest that adding $ZnCl_2$ to the $CuInS_2$ nanoclusters allows the simultaneous introduction of Zn into the $CuInS_2$ lattice structure while conversion of the clusters into a crystalline metal chalcogenide phase.

Figure 6a shows a digital photograph of the CuInZnS with different molar precursor ratios of Zn/In. Excitation of the nanocrystal samples with a UV-lamp shows intense PL emission. The PL intensity gradually increases as more Zn is incorporated into the $CuInS_2$ nanocrystals. Moreover, increasing the Zn^{2+} content shifts the UV-Vis absorption edge to shorter wavelengths (Figure 6b). The bulk band gaps of ZnS and In_2S_3 are 3.7 eV and 2.1 eV, respectively.[52] The blue shift observed for higher Zn/In ratio has been previously reported, and was explained by the fact that the presence of higher band gap material is responsible for increasing the overall band gap of the alloyed nanocrystal.[52] On the other hand, the overall band gap of the alloyed nanocrystals tends to decrease with increased content of lower band gap material.[52] When Zn is incorporated into the $CuInS_2$, the PL intensity increases and shows well-defined peaks (Figure 6c). More importantly, the ratio of intensity to FWHM of the PL emission peaks does not increase with increasing Zn content. This clearly indicates that the PL emission (and increase in intensity) is mainly due to the incorporation of Zn in the $CuInS_2$ lattice, rather than due to separately-formed ZnS nanoparticles. Unlike previous reports, our result indicates that we have achieved successful control of the reactivity of all cationic precursors and prevented independent nucleation.[69] The presence of more Zn ions introduces lattice dislocations, causing much higher PL intensity.[53] At higher Zn/In molar ratios, surface passivation can be expected. Introduction of Zn to $CuInS_2$ and possible surface passivation therefore causes a pronounced increase in intensity of PL spectra.[52,70] Figure 6d shows the effect of Zn/Cu molar ratio on the PL intensity and PL peak position. It can be clearly seen that increasing the Zn/Cu molar ratio dramatically increases the PL intensity and shifts PL peak position to smaller wavelengths.

While the incorporation of Zn was achieved by introducing Zn^{2+} after forming $CuInS_2$ nanoclusters, our method also affords the opportunity to introduce guest cations during the formation of nanoclusters (stage 1). Because our nanocluster precursor is formed at a low temperature, cations introduced in the cluster formation stage can be incorporated into the nanoclusters directly to produce the desired metal ion doped $CuInS_2$ monomer. The ability to include guest ions in the cluster formation stage is mainly due to the high reactivity of $(NH_4)_2S$, which facilitates the low temperature reaction with cations such as Ga^{3+} and In^{3+}. In order to systematically study this phenomenon, $GaCl_3$ was used to prepare the $CuInGaS_2$ nanoclusters. Using the same reaction conditions used for $CuInS_2$ nanocrystals, the $CuInGaS_2$ nanoclusters were crystallized to form $CuInGaS_2$ nanocrystals. To aid the incorporation of Ga, we prepared In-deficient $CuInS_2$. Compared to the Cu-deficient $CuInS_2$, In-deficient $CuInS_2$ did not exhibit interesting PL emission properties. The molar ratio of Ga/Cu was varied to understand the structural and optical properties of $CuInGaS_2$ nanoparticles. Figure 7a shows a TEM image of as-prepared $CuInGaS_2$, which has a Cu:Ga starting molar ratio of 1:0.2. As-synthesized $CuInGaS_2$ nanocrystals exhibit a

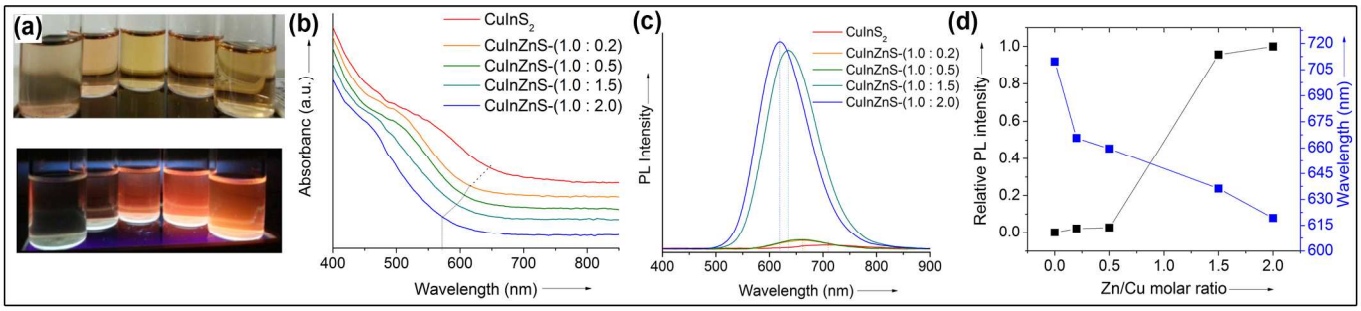

Figure 6. a) Photograph of CuInZnS in hexane and corresponding picture under 240 nm excitation. The Zn content in the CuInZnS samples increase from left to right. b) Absorption and c) PL spectra of as prepared CuInZnS with different Cu:Zn precursor molar ratios. d) PL intensity and wavelength dependence of Cu:Zn starting molar ratios (Optical absorption of all samples at 400 nm is set to 1.0).

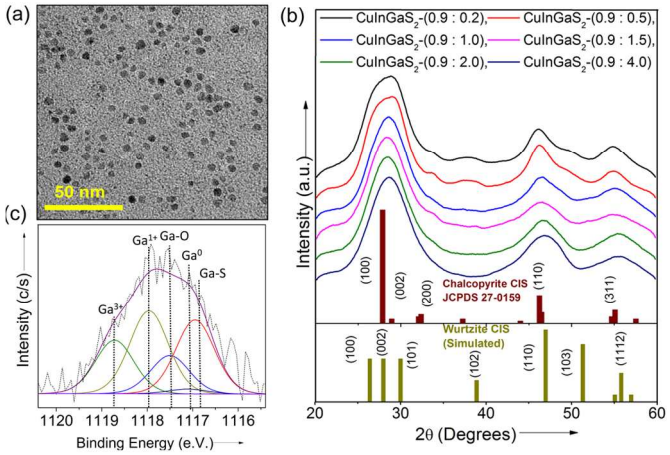

Figure 7. a) TEM image of $CuInGaS_2$ nanoparticles. b) XRD patterns of $CuInGaS_2$ with different Ga/Cu molar ratios. Dash line shows the peak shift of (110) reflection. c) XPS spectra of Ga 2p.

spherical morphology and have an average diameter of 5.65±0.81 nm. Figure 7b shows XRD patterns of as-synthesized $CuInGaS_2$ with a series of broad peaks corresponding to the chalcopyrite crystal structure. Varying the Ga/Cu molar ratio results in similar diffraction patterns; however, as the molar ratio of Ga/Cu is increased three main characteristic features can be isolated from the XRD patterns. First, the most intense peak (100) becomes sharper and more symmetric. Second, the intensity of wurtzite phase (102) peak diminishes in samples having higher Ga/Cu molar ratios. Third, the chalcopyrite phase (110) peak gradually shifts to a higher 2θ angle. The combination of the smaller size of the nanocrystals and the mixed phases of chalcopyrite and wurtzite both contribute to the peak broadening in these samples. In particular, the chalcopyrite and wurtzite (100), (002), and (101) peaks are present and overlapping in 20 – 30° 2θ range. Thus, the broadening of (100) peak is evidence of the polytypism of the wurtzite and chalcopyrite phases within the crystal structure. According to our observations, increasing the Ga/Cu molar ratio alters the phase from polytypic to chalcopyrite. This effect is further confirmed by the gradual decrease of the intensity of (102) peak. Since the (100) peak is susceptible to peak broadening, the peak shift of the (110) plane exhibits a more pronounced shift toward a higher 2θ angle. On the basis of observation above, we conclude that Ga is incorporated during the formation of the monomer. We assume that excess Ga precursor is removed during the isolation and cleaning of the monomer. Thus, in the second stage, the Ga-incorporated $CuInS_2$ nanoclusters are nucleated to grow nanocrystals. The chemical nature of Ga in $CuInGaS_2$ was analyzed using the XPS spectrum of Ga $2p_{3/2}$ core electrons, which are located at 1117.8 eV (Figure 7c). De-convoluted peaks illustrate the agreement between experimental and fitted data. XPS peaks corresponding to Ga^{3+}, Ga^{1+}, Ga-S, Ga-O and metallic type Ga electrons are located at 1118.7, 1118, 1117.02 and 1117.4 eV, respectively.[71] However, the majority of the bonds are associated with the oxidation states of Ga^{1+}, Ga^{3+}, and Ga-S bonds. This experimental evidence confirms the incorporation of Ga^{3+} within the $CuInS_2$ structure in the nanocrystals. Figure 8a shows the evolution of optical spectra of $CuInGaS_2$ with increasing Ga/Cu molar ratio. Upon increasing the Ga content, a blue shift of the absorption wavelength from 542.9 nm to 494.2 nm was observed. Because this is a two-step synthesis, we are able to incorporate different cations during both nanocluster formation and nucleation stages. This capability was investigated by successfully introducing both Ga and Zn during the cluster preparation and nucleation/growth stages: first the $CuInGaS_2$ nanoclusters are prepared, then the Zn^{2+} is introduced during the nucleation/growth step to obtain Zn-$CuInGaS_2$. The onset band gap of $CuInS_2$ increased with the incorporation of Ga^{3+}. The measured band gap of $CuInGaS_2$ with Ga/Cu molar ratios of 0, 0.5, 1.0, 2.0 and 4.0 are 1.87, 1.9, 2.0, 2.1 and 2.17 eV, respectively.

To synthesize Zn-$CuInGaS_2$ nanocrystals, the $CuInGaS_2$ nanoclusters are formed with different initial Ga/Cu ratios, and Zn (Zn:In-1:1) is introduced during the crystallization step. Figure 8b shows a digital photograph of Zn-$CuInGaS_2$ increasing the Ga content from left to right and the PL activity under the UV radiation of UV light (390 nm excitation wavelength). A significant blue shift of the absorption spectra was observed with increasing the starting Ga/Cu molar ratio in the nanoclusters and subsequent introduction of Zn during the second stage (Figure 8c). In order to understand the behavior of the Ga/Cu molar ratio, the ratio of Zn/In is kept constant (1:1). The absorbance onset was determined by least-squares fit of the linear region of the UV spectra (Figure s5). Band gaps corresponding to the Zn-$CuInGaS_2$ with starting molar ratio of Ga/Cu-0.5, 1.0, 1.5, 2.0 and 4.0 were shifted to 2.15, 2.24, 2.27, 2.30 and 2,53 eV, respectively. The effect of Zn on the band gap of $CuInGaS_2$ is further illustrated in Figure 8d. These results further confirm that the presence of both Ga and Zn increases the band gap of $CuInS_2$. The synergistic effect of both Zn and Ga incorporation is elaborated in Figure s6 (a, b). Compared to the pure $CuInS_2$, both the CuInZnS and $CuInGaS_2$ nanocrystals show a blue shift in the optical absorption spectra. Compared to CuInZnS and $CuInGaS_2$, the largest blue shift in the absorption edge corresponds to the Zn-$CuInGaS_2$ sample. This can be attributed to the synergistic effect of decreasing the absorption wavelength of both CuInZnS and $CuInGaS_2$ nanocrystals.

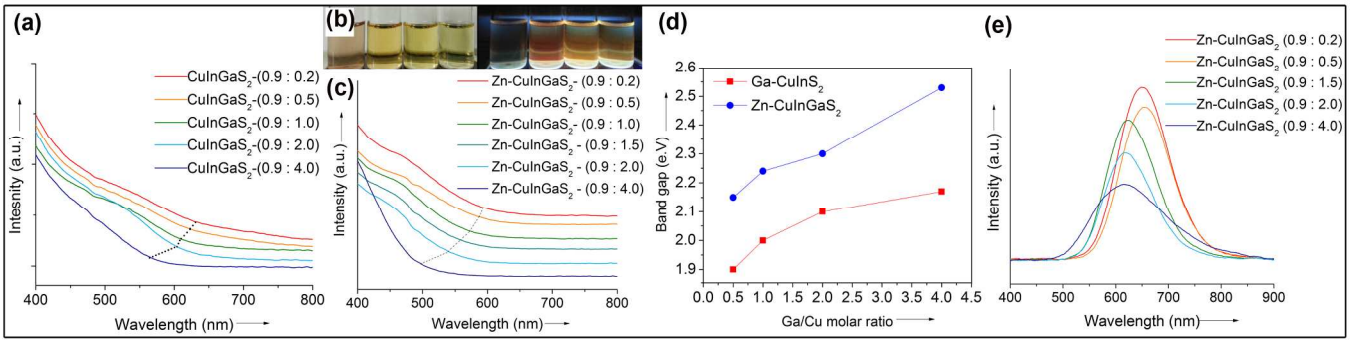

Figure 8. a) UV-vis absorption of as prepared $CuInGaS_2$ prepared with different molar ratios of Cu:Ga. Ratios in the formula denote the starting molar ratios of Cu:Ga. b) Digital photographs of Zn-$CuInGaS_2$ samples before and after irradiating with UV-light (390 nm excitation wavelength), showing the PL emission of Zn-$CuInGaS_2$. Going from left to right, the Ga/Cu initial molar ratio is increased while keeping the initial Zn/In (1:1) ratio constant. c) UV-vis absorption of as prepared Zn-$CuInGaS_2$. d) Synergistic effect of Zn on the band gap of $CuInGaS_2$ prepared with different Cu:Ga molar ratios. e) PL emission spectra of $CuInGaS_2$ with different Cu:Ga molar ratios.. All PL spectra were acquired after adjusting the particle concentration such that the optical absorption at 400 nm was 1.0.

The dependence of the PL intensity and emission wavelength with the ratio of Cu:Ga is shown in Figure 8e. At first, it increases rapidly with increasing Ga content. In Ga-rich particles PL intensity then decreases systematically. The highest PL intensity was observed for the Zn-$CuInGaS_2$-(0.9 : 0.2) sample. As seen in previous studies for $CuInGaSe_2$, nanocrystals with higher ratios of Ga/Cu may tend to aggregate, thus leading to a decrease in the PL intensity.[5]

Conclusions

We have developed a simple two-step process to synthesize nanocrystals of $CuInS_2$ with different morphologies and phases. First, cationic precursors are treated with $(NH_4)_2S$ at 60 ^oC and a $CuInS_2$ nanocluster species is prepared. These nanoclusters act as a precursor for nucleation and crystal growth of $CuInS_2$ nanocrystals. Heating the nanoclusters in the presence of DDT to 145 ^oC (3 ^oC/min rate) yields spherical $CuInS_2$ q-dots (quantum dots). The presence of a small amount of TOP directs the nanoclusters to grow into nanodisks. Heating-up the nanoclusters rapidly to 160 ^oC (10 ^oC/min rate) produces nanorods. We observe different phases of $CuInS_2$ under these two heating up conditions: q-dots and nanodisks exhibit the chalcopyrite phase while nanorods exhibit the wurtzite phase. Incorporation of Ga as a starting material forms $CuInGaS_2$ nanoclusters, and subsequent crystallization leads to the formation of $CuInGaS_2$ nanocrystals. $CuInGaS_2$ shows enhanced optical emission and a shift in the absorption spectra to shorter wavelengths. A similar phenomenon was observed in the optical properties when introducing Zn to the $CuInS_2$ monomer. Finally, we were able introduce Zn to $CuInGaS_2$ clusters to form pentanary Zn-$CuInGaS_2$ nanocrystals. A synergistic effect in the UV-vis absorption spectra was observed when both Zn and Ga are present. The isolation of the intermediate $CuInS_2$ nanoclusters is a favorable protocol to understand the formation of a wide variety of ternary, quaternary, and pentanary chalcogenides.

Acknowledgements

This work was supported in part by the National Science Foundation (NSF) under award number CMMI-1344562. This work made use of the Cornell Center for Materials Research Shared Facilities, which are supported through the NSF MRSEC program (DMR-1120296).

Notes and references

1. R. D. Robinson, B. Sadtler, D. O. Demchenko, C. K. Erdonmez, L.-W. Wang and A. P. Alivisatos, *Science*, 2007, 317, 355-358.
2. M. Danek, K. F. Jensen, C. B. Murray and M. G. Bawendi, *Chem. Mater.*, 1996, 8, 173-180.
3. D. Yu, C. Wang and P. Guyot-Sionnest, *Science*, 2003, 300, 1277-1280.
4. V. L. Colvin, M. C. Schlamp and A. P. Allvisatos, *Nature*, 1994, 370, 354-357.
5. M. G. Panthani, V. Akhavan, B. Goodfellow, J. P. Schmidtke, L. Dunn, A. Dodabalapur, P. F. Barbara and B. A. Korgel, *J. Am. Chem. Soc.*, 2008, 130, 16770-16777.
6. S.-Z. Kang, Y.-K. Yang, W. Bu and J. Mu, *J. Solid State Chem.*, 2009, 182, 2972-2976.
7. H. Zhong, Z. Bai and B. Zou, *J. Phys. Chem. Lett.*, 2012, 3, 3167-3175.
8. K. Yu, P. Ng, J. Ouyang, M. B. Zaman, A. Abulrob, T. N. Baral, D. Fatehi, Z. J. Jakubek, D. Kingston, X. Wu, X. Liu, C. Hebert, D. M. Leek and D. M. Whitfield, *ACS Appl. Mater. Interfaces*, 2013, 5, 2870-2880.
9. S. Buhbut, S. Itzhakov, I. Hod, D. Oron and A. Zaban, *Nano Lett.*, 2013, 13, 4456-4461.
10. K. P. Rice, A. E. Saunders and M. P. Stoykovich, *J. Am. Chem. Soc.*, 2013, 135, 6669-6676.
11. K. Tarafder, Y. Surendranath, J. H. Olshansky, A. P. Alivisatos and L. W. Wang, *J. Am. Chem. Soc.*, 2014, 136, 5121-5131.
12. J. E. Halpert, V. J. Porter, J. P. Zimmer and M. G. Bawendi, *J. Am. Chem. Soc.*, 2006, 128, 12590-12591.
13. I. Gur, N. A. Fromer, M. L. Geier and A. P. Alivisatos, *Science*, 2005, 310, 462-465.

14. W. U. Huynh, J. J. Dittmer and A. P. Alivisatos, *Science*, 2002, 295, 2425-2427.

15. D. Wang, W. Zheng, C. Hao, Q. Peng and Y. Li, *Chem. Commun.*, 2008, 2556-2558.

16. B. Mao, C.-H. Chuang, F. Lu, L. Sang, J. Zhu and C. Burda, *J. Phys. Chem. C*, 2013, 117, 648-656.

17. Q. Guo, G. M. Ford, H. W. Hillhouse and R. Agrawal, *Nano Lett.*, 2009, 9, 3060-3065.

18. S. N. Malik, S. Mahboob, N. Haider, M. A. Malik and P. O'Brien, *Nanoscale*, 2011, 3, 5132-5139.

19. X. Yu, X. An, A. Shavel, M. Ibáñez and A. Cabot, *J. Mater. Chem. A*, 2014, 2, 12317-12322.

20. S. L. Castro, S. G. Bailey, R. P. Raffaelle, K. K. Banger and A. F. Hep, *Chem. Mater.*, 2003, 15, 3142-3147.

21. N. Zheng, X. Bu and P. Feng, *Nature*, 2003, 426, 428-432.

22. Y. Qi, Q. Liu, K. Tang, Z. Liang, Z. Ren and X. Liu, *J. Phys. Chem. C*, 2009, 113, 3939-3944.

23. D. Aldakov, A. Lefrançois and P. Reiss, *J. Mater. Chem. C*, 2013, 1, 3756-3776.

24. L. Yi, Y. Liu, N. Yang, Z. Tang, H. Zhao, G. Ma, Z. Su and D. Wang, *Energy & Env. Sci.*, 2013, 6, 835-840.

25. Z. Peng, Y. Liu, W. Shu, K. Chen and W. Chen, *Eur. J. Inorg. Chem.*, 2012, 2012, 5239-5244.

26. W. Chung, H. Jung, C. H. Lee and S. H. Kim, *OPTICS EXPRESS*, 2012, 20, 25071-25076.

27. J. Xiao, Y. Xie, R. Tang and Y. Qian, *J. Solid State Chem.*, 2001, 161, 179-183.

28. Y. Wang, X. Zhao, F. Liu, X. Zhang, H. Chen, F. Bao and X. Liu, *RSC Advances*, 2014, 4, 16022-16026.

29. M. E. Norako, M. A. Franzman and R. L. Brutchey, *Chem. Mater.*, 2009, 21, 4299-4304.

30. B. Chen, H. Zhong, W. Zhang, Z. a. Tan, Y. Li, C. Yu, T. Zhai, Y. Bando, S. Yang and B. Zou, *Adv. Funct. Mater.*, 2012, 22, 2081-2088.

31. L. Carbone, C. Nobile, M. D. Giorgi, F. D. Sala, G. Morello, P. Pompa, M. Hytch, E. Snoeck, A. Fiore, I. R. Franchini, M. Nadasan, A. F. Silvestre, L. Chiodo, S. Kudera, R. Cingolani, R. Krahne and L. Manna, *Nano Lett.*, 2007, 7, 2942-2950.

32. M. Uehara, K. Watanabe, Y. Tajiri, H. Nakamura and H. Maeda, *J Chem Phys*, 2008, 129, 134709.

33. L. De Trizio, M. Prato, A. Genovese, A. Casu, M. Povia, R. Simonutti, M. J. P. Alcocer, C. D'Andrea, F. Tassone and L. Manna, *Chem. Mater.*, 2012, 24, 2400-2406.

34. G. Manna, S. Jana, R. Bose and N. Pradhan, *J. Phys. Chem. Lett.*, 2012, 3, 2528-2534.

35. S. Jana, B. B. Srivastava, S. Jana, R. Bose and N. Pradhan, *J. Phys. Chem. Lett.*, 2012, 3, 2535-2540.

36. Y. Chen, S. Li, L. Huang and D. Pan, *Inorg. Chem.*, 2013, 52, 7819-7821.

37. M. Booth, A. P. Brown, S. D. Evans and K. Critchley, *Chem. Mater.*, 2012, 24, 2064-2070.

38. S. K. Batabyal, L. Tian, N. Venkatram, W. Ji and J. J. Vittal, *J. Phys. Chem. C*, 2009, 113, 15037-15042.

39. N. Bao, X. Qiu, Y. H. Wang, Z. Zhou, X. Lu, C. A. Grimes and A. Gupta, *Chem. Commun.*, 2011, 47, 9441-9443.

40. Z. Yin, Z. Hu, H. Ye, F. Teng, C. Yang and A. Tang, *Appl. Surf. Sci.*, 2014, 307, 489-494.

41. D. Pan, L. An, Z. Sun, W. Hou, Y. Yang, Z. Yang and Y. Lu, *J. Am. Chem. Soc.*, 2008, 130, 5620-5621.

42. H. Zhong, S. S. Lo, T. Mirkovic, Y. Li, Y. Ding, Y. Li and G. D. Scholes, *ACS Nano*, 2010, 4, 5253-5262.

43. B. Koo, R. N. Patel and B. A. Korgel, *Chem. Mater.*, 2009, 21, 1962-1966.

44. S.-H. Choi, E.-G. Kim and T. Hyeon, *J. Am. Chem. Soc.*, 2006, 128, 2520-2521.

45. S. T. Connor, C.-M. Hsu, B. D. Weil, S. Aloni and a. Y. Cui, *J. Am. Chem. Soc.*, 2009, 131, 4962-4966.

46. H. Zhang, L. V. Solomon, D. H. Ha, S. Honrao, R. G. Hennig and R. D. Robinson, *Dalton Trans.*, 2013, 42, 12596-12599.

47. H. Zhang, B. R. Hyun, F. W. Wise and R. D. Robinson, *Nano Lett.*, 2012, 12, 5856-5860.

48. E. Dilena, Y. Xie, R. Brescia, M. Prato, L. Maserati, R. Krahne, A. Paolella, G. Bertoni, M. Povia, I. Moreels and L. Manna, *Chem. Mater.*, 2013, 25, 3180-3187.

49. Y.-K. Kim, S.-H. Ahn, K. Chung, Y.-S. Cho and C.-J. Choi, *J. Mater. Chem.*, 2012, 22, 1516-1520.

50. J. Seo, S. Raut, M. Abdel-Fattah, Q. Rice, B. Tabibi, R. Rich, R. Fudala, I. Gryczynski, Z. Gryczynski, W.-J. Kim, S. Jung and R. Hyun, *J. Appl. Phys.*, 2013, 114, 094310.

51. Q. Liu, R. Deng, X. Ji and D. Pan, *Nanotechnology*, 2012, 23, 255706.

52. W. Zhang, Q. Lou, W. Ji, J. Zhao and X. Zhong, *Chem. Mater.*, 2014, 26, 1204-1212.

53. X. Tang, W. Cheng, E. S. Choo and J. Xue, *Chem. Commun.*, 2011, 47, 5217-5219.

54. T. Wu, Q. Zhang, Y. Hou, L. Wang, C. Mao, S. T. Zheng, X. Bu and P. Feng, *J. Am. Chem. Soc.*, 2013, 135, 10250-10253.

55. W. Hirpo, S. Dhingra and M. G. Kanatzidis, *J. Chem. Soc., Chem. Commun.*, 1992, 557-559.

56. G. Henkel, B. Krebs, P. Betz, H. Fietz and K. Saatkarnp, *Angew. Chem. Int. Ed. Engl.*, 27, 1326-1329.

57. H. Zhong, Y. Zhou, M. Ye, Y. He, J. Ye, C. He, C. Yang and Y. Li, *Chem. Mater.*, 2008, 20, 6434-6443.

58. T. Omata, K. Nose, K. Kurimoto and M. Kita, *J. Mater. Chem. C*, 2014, 2, 6867-6872.

59. B. Huang, Q. Dai, N. Zhuo, Q. Jiang, F. Shi, H. Wang, H. Z. C. Liao, Y. Cui and J. Zhang, *J. Appl. Phys.*, 2014, 116, 094303.

60. K. Das, S. K. Panda and S. G. P. M. S. Chaudhuri, *Mater. Res. Bull*, 2007, 43, 2742-2750.

61. J.-J. He, W.-H. Zhou, J. Guo, M. Li and S.-X. Wu, *Cryst. Eng. Comm.*, 2012, 14.

62. H. Wu and W. Chen, *Nanoscale*, 2011, 3, 5096-5102.

63. K. Nose, Y. Soma, T. Omata and S. Otsuka-Yao-Matsuo, *Chem. Mater.*, 2009, 21, 2607-2613.

64. F. Wang, V. N. Richards, S. P. Shields and W. E. Buhro, *Chem. Mater.*, 2014, 26, 5-21.

65. A. B. F. Martinson, S. C. Riha, E. Thimsen, J. W. Elam and M. J. Pellin, *Energy & Env. Sci.*, 2013, 6, 1868-1878.

66. J. Kolny-Olesiak and H. Weller, *ACS Appl. Mater. Interfaces*, 2013, 5, 12221-12237.

67. D. Aldakov, A. Lefrançois and P. Reiss, *J. Mater. Chem. C*, 2013, 1, 3756.

68. V. T. Tiong, Y. Zhang, J. Bell and H. Wang, *CrystEngComm*, 2014, 16, 4306-4313.

69. L. Li, T. J. Daou, I. Texier, T. T. K. Chi, N. Q. Liem and P. Reiss, *Chem. Mater.*, 2009, 21, 2422–2429.

70. W.-S. Song, E.-P. Jang, J.-H. Kim, H. S. Jang and H. Yang, *J. Nanopart. Res.*, 2013, 15, 15.

71. S. McDonnell, H. Dong, J. M. Hawkins, B. Brennan, M. Milojevic, F. S. Aguirre-Tostado, D. M. Zhernokletov, C. L. Hinkle, J. Kim and R. M. Wallace, *Appl. Phys. Lett.*, 2012, 100, 141606.